

# Flexoelectric electricity generation by crumpling graphene

Cite as: J. Appl. Phys. **129**, 225107 (2021); <https://doi.org/10.1063/5.0052482>

Submitted: 31 March 2021 . Accepted: 19 May 2021 . Published Online: 14 June 2021

 Brahmanandam Javvaji,  Ranran Zhang,  Xiaoying Zhuang, and Harold S. Park



View Online



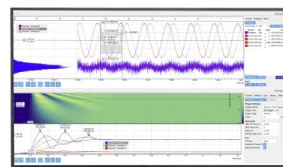
Export Citation



CrossMark

## Challenge us.

What are your needs for  
periodic signal detection?



Zurich  
Instruments



# Flexoelectric electricity generation by crumpling graphene

Cite as: J. Appl. Phys. **129**, 225107 (2021); doi: 10.1063/5.0052482

Submitted: 31 March 2021 · Accepted: 19 May 2021 ·

Published Online: 14 June 2021



Brahmanandam Javvaji,<sup>1</sup> Ranran Zhang,<sup>1</sup> Xiaoying Zhuang,<sup>1,2,a)</sup> and Harold S. Park<sup>3</sup>

## AFFILIATIONS

<sup>1</sup>Computational Science and Simulation Technology, Institute of Photonics, Faculty of Mathematics and Physics, Leibniz Universität Hannover, Appelstr. 11A, 30167 Hannover, Germany

<sup>2</sup>Department of Geotechnical Engineering, College of Civil Engineering, Tongji University, 1239 Shanghai 200092, China

<sup>3</sup>Department of Mechanical Engineering, Boston University, Boston, Massachusetts 02215, USA

**Note:** This paper is part of the Special Topic on Trends in Flexoelectricity.

**a)** Author to whom correspondence should be addressed: [zhuang@iop.uni-hannover.de](mailto:zhuang@iop.uni-hannover.de)

## ABSTRACT

We utilize atomistic simulations that account for point charges and dipoles to demonstrate that flexoelectricity, which arises from strain gradients, can be exploited to generate electricity from crumpled graphene sheets. Indentation of a circular graphene sheet generates localized developable (d)-cones, for which we verify the core radius and azimuthal angle with established theoretical models. We determine the voltage that can be generated based on the resulting electrostatic fields and compare the voltage generation to previous theoretical predictions that are scaled down to the nanoscale. In doing so, we find that the voltage generated from crumpling graphene exceeds, by about an order of magnitude, the expected voltage generation, indicating the benefit of exploiting the large strain gradients that are possible at the nanoscale. Finally, we demonstrate that crumpling may be a superior mechanism of flexoelectric energy generation as compared to bending of two-dimensional nanomaterials.

Published under an exclusive license by AIP Publishing. <https://doi.org/10.1063/5.0052482>

## I. INTRODUCTION

Two-dimensional (2D) nanomaterials have been widely studied because of their novel physical properties.<sup>1–11</sup> An emerging application area for 2D materials is that of electromechanical energy generation<sup>12–18</sup> due to their potential for nanoscale energy harvesting and generation.<sup>19,20</sup> In this vein, piezoelectricity, the best-known mechanism for converting mechanical deformation into electrical energy, has been studied in 2D materials.<sup>21–23</sup> In contrast, flexoelectricity, for which the polarization of the material depends upon the strain gradient, has been less studied as an energy generation and conversion mechanism for 2D materials.<sup>23–29</sup> Because flexoelectricity depends on the strain gradient, it is, unlike piezoelectricity, theoretically possible in any material and has been recently studied in 2D materials.

Graphene is a centrosymmetric material that does not exhibit piezoelectricity.<sup>30,31</sup> However, bending graphene can induce a change in hybridization from  $sp^2$  to  $sp^3$ , where the valence electrons of the carbon atoms develop bonding interactions with the neighboring

bonded electrons ( $\pi - \sigma$  interactions).<sup>32</sup> This change in bonding due to strain gradients from bending leads to the generation of electrical polarization via local electric fields and thus the emergence of flexoelectricity.<sup>12</sup> Flexoelectricity has also been reported in other 2D materials.<sup>17</sup> For example, the monolayer transition metal dichalcogenides (TMDCs) exhibit a flexoelectric response that is one order of magnitude higher than graphene.<sup>12</sup> Furthermore, Janus TMDCs show exceptional bending flexoelectric properties related to the initial degree of asymmetry<sup>13</sup> and exhibit flexoelectric constants that exceed graphene and TMDCs. The flexoelectric properties of other recently synthesized monolayers have also been investigated.<sup>16,33,34</sup> These recent studies have demonstrated the promising potential of 2D materials for flexoelectric energy generation and conversion.

Here, we investigate the potential for generating electricity by crumpling 2D materials, specifically graphene. This work is motivated by recent experimental studies on electrical power generation by crumpling thin polymer films<sup>35</sup> and theoretical works on flexoelectric energy generation by crumpling thin sheets, such as paper,<sup>36</sup> in which electricity was produced via the flexoelectric effect by

crumpling thin circular sheets supported on a hoop via central forces created by a cone tip. Of specific interest is the formation of a developable (d)-cone during the indentation, as the simplest example of thin sheet crumpling, which generates strain gradients and thus the development of electrical polarization and voltage. Here, we examine the potential of crumpling atomically thin sheets, specifically monolayer graphene, as a means of electromechanical energy generation at the nanoscale. We do this via classical molecular dynamic simulations that account for point charges and dipoles to investigate the mechanisms driving the voltage generated from the indentation, and subsequent crumpling, of a monolayer graphene sheet.

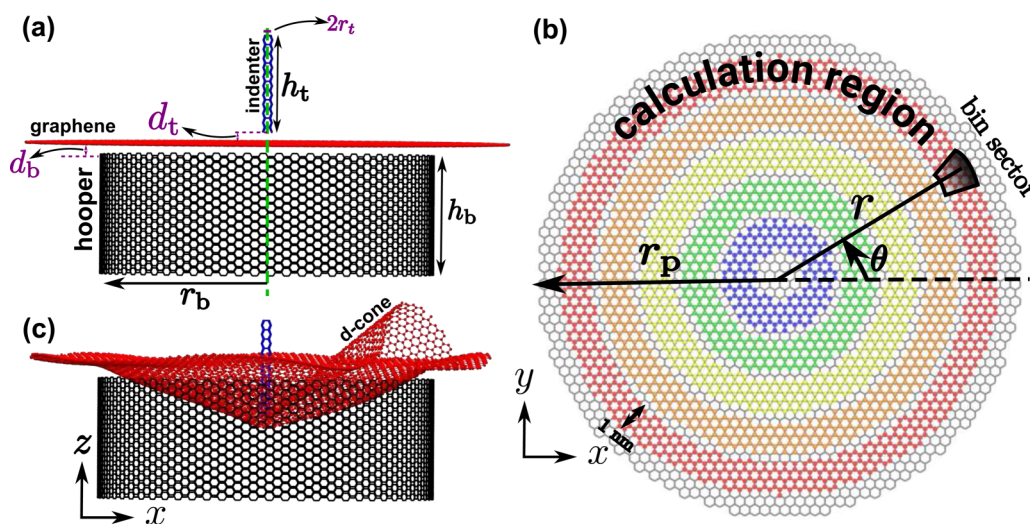
## II. SIMULATION METHOD

Figure 1(a) shows the simulation setup used to conduct the atomistic simulations. We consider a circular graphene sheet (CGS) of radius  $r_p$  placed on top of a carbon nanotube (CNT) of radius  $r_b$  with height  $h_b$  at a distance of  $d_b$ . This CNT acts as a supporting hoop (called the hooper) for the CGS. Another CNT, which is used to indent the CGS, with radius  $r_t$  and height  $h_t$ , is initially located at a distance  $d_t$  from the CGS. The interatomic forces acting on each atom in the CGS were calculated using a combination of short-range bonded interactions and long-ranged charge-dipole (CD) interactions. The AIREBO potential<sup>37</sup> was employed to account for the short-range bonded interactions, while for the CD interactions, each atom is assumed to carry a charge  $q$  and dipole moment  $\mathbf{p}$ .<sup>38,39</sup> The minimization of charge-charge, charge-dipole, and dipole-dipole interactions to the total system energy leads to the governing equations for obtaining the charge and dipole moments for each atom. The complete details about the implementation of the CD model in conjunction with a classical molecular dynamics (MD) simulation can be found in our previous

works.<sup>12,31</sup> All the simulations in this work were conducted using the open-source MD code LAMMPS.<sup>40</sup> The visual molecular dynamics (VMD) package<sup>41</sup> has been used to generate the atomic snapshots.

The interactions between the CGS and both CNTs (the indenter and hooper) were limited to van der Waals forces to avoid bonded interactions between the CGS and CNTs, where the van der Waals forces were modeled using a Lennard-Jones potential.<sup>42</sup> In the initial simulation setup,  $d_b$  and  $d_t$  are set as 0.33 nm at which the CGS and the CNTs have minimum potential energy and thus no interaction forces. Both the CNT hooper and CNT indenter are modeled as rigid bodies, while the CGS is allowed to slide, via the van der Waals forces, over the CNT hooper in response to the CNT indenter. The CNT hooper is fixed spatially throughout the indentation process.

The CGS was initially equilibrated using the Nosé-Hoover thermostat<sup>43,44</sup> for about 100 000 steps with a time step of 0.5 fs at a temperature of 0.1 K to minimize thermal fluctuations. The indenter CNT moves with a speed of 0.02 nm/ps toward the CGS, where the atomic positions are integrated forward in time using a standard velocity Verlet algorithm.<sup>45</sup> The atomic coordinates along with the charge and dipole data are collected at every 1000 steps during the time integration. We vary the CGS radius ( $r_p$ ) from 7 to 10 nm to study the effect of the graphene sheet size during the crumpling deformation and the resultant voltage generation. However, we varied the radius of both the indenter and hooper CNTs to ensure the same percentage of the CGS is indented, regardless of CGS diameter. About 25% of CGS atoms are supported by the hooper and 0.025% of CGS atoms are indented by the top CNT. The 100-fold reduction in the indented atoms as compared to the supported atoms is to mimic a sharp indenter tip.



**FIG. 1.** (a) Schematic of the circular graphene sheet supported on CNT for deformation by indentation. (b) In-plane view of the setup in (a). Region used for calculation highlighted with red color. Within this region, several bin sectors were constructed to evaluate physical quantities of interest. (c) Represents the d-cone formation under indentation.

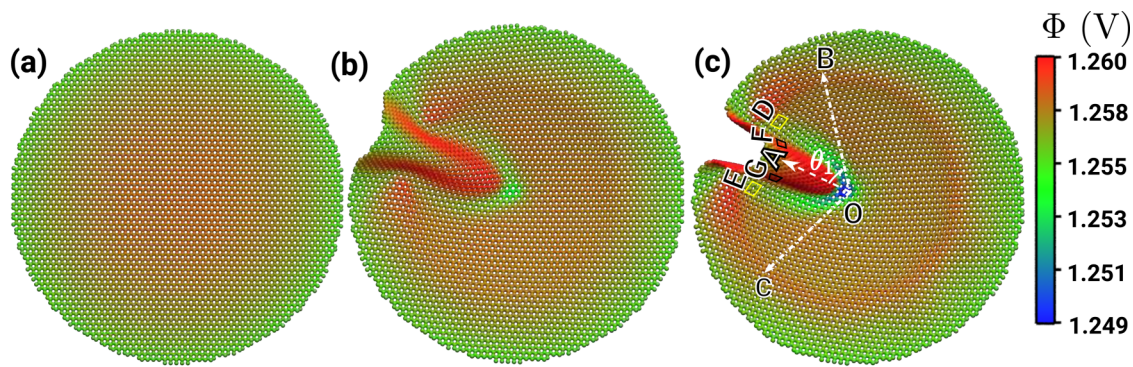


**FIG. 2.** Atomic snapshots of the 9 nm CGS when the indentation depth is (a) 0, (b) 1.546, and (c) 2.541 nm. Atoms in (a)–(c) are colored using the electrostatic potential  $\Phi$  for 9 nm CGS. Note the development of the d-cone in (b) and (c). Labels O, A, B, and C represent the CGS center or d-cone core, the d-cone tip, and the edges of the d-cone, respectively. D, E, F, and G denote the atom bins nearer to bin A. OA represents the bin sector with the largest  $z$  deflection and for this bin, we set  $\theta$  as  $0^\circ$ .  $\theta_1$  is the angle between OA and either OB or OC.

We define several circular regions starting from the center of the CGS. These regions have a width of about 1 nm and radius  $r$  varying from 1 to  $r_p - 2$  nm, as shown in Fig. 1(b). Furthermore, each region is subdivided into 60 bin sectors as highlighted in Fig. 1(b). For these sectors, we averaged the atomic coordinates, potential energy, voltage, charges, and dipole moments at a series of indentation steps. The local curvature  $\kappa$  of the bin sector is estimated from the derivatives of spline interpolations with respect to the averaged  $x$  and  $y$  coordinates of each bin. At each indentation step, we consider the atoms with minimum  $z$ -coordinates near to the core portion of the developable (d)-cone to define the center of the CGS, which is labeled “O” in Fig. 2(c). Those atoms are used for measuring the depth and inner voltage  $\Phi_O$ . The tip deflection is the difference between the initial and indented  $z$ -coordinates for atoms associated with O. Figure 1(c) represents the d-cone formation due to the indentation of CGS.

We define two dimensionless parameters to aid in the analysis. The dimensionless parameter  $\alpha_1$  is the ratio between depth and  $r_b$ , which can be interpreted as the dimensionless tip deflection. Another dimensionless parameter  $\alpha_2 = R_c/r_b$ , where  $R_c$  is the core radius, and so  $\alpha_2$  can be interpreted as the dimensionless core radius. Using these two parameters, we further compare our simulation results with the earlier reported models,<sup>36</sup> which were performed at significantly larger length scales. Finally, we note that the electromechanical energy density is defined as the sum of the dot product between the polarization and the electric fields over the CGS area, while the strain energy density is the scalar valued tensor product of atomic stress and atomic strain over the same area of the CGS. The electromechanical energy density is equal to the electrical energy density stored in an energy harvester when subjected only to mechanical loads.<sup>46–48</sup>

### III. RESULTS AND DISCUSSION

#### A. Verification of crumpling simulations

We first demonstrate that our atomistic simulations of graphene crumpling follow previous theoretical results.<sup>36,49,50</sup>

The initial thermally equilibrated atomic configuration of the CGS in Fig. 2(a) shows small out-of-plane fluctuations near the edges, as expected as the edges are not fixed. The low system temperature of 0.1 K suppresses large edge fluctuations or ripples, which have an amplitude of 0.1 nm in the  $z$ - (out of plane) direction. The indentation induces deformation at the center of the CGS, which through bond bending and stretching extends to deform the rest of the CGS. Figure 2(b) clearly indicates a non-uniform change of out-of-plane displacements in a confined portion of CGS. Further indentation increases the deformation and the atomic configuration in Fig. 2(c) clearly shows the formation of a developable cone (d-cone) due to crumpling.

The deformation in the graphene sheet changes the local electrostatic fields and thus induces polarization by altering the charges and dipole moments through piezoelectricity and flexoelectricity. However, due to the absence of piezoelectricity in graphene, the only electrical response we can measure is due to flexoelectricity. The governing equation for the charges  $q$  and dipoles  $\mathbf{p}$  in the charge-dipole model is<sup>12</sup>

$$T_{ii}^{q-q} q_i + \sum_{j,i \neq j}^N T_{ij}^{q-q} q_j - \sum_{j,i \neq j}^N \mathbf{T}_{ij}^{q-p} \mathbf{p}_j = \chi_i. \quad (1)$$

From Eq. (1), the electrostatic potential  $\Phi$  associated with each atom is written as

$$\Phi_i = T_{ii}^{q-q} q_i = [\Phi_i^p + \Phi_i^q + \chi_i], \quad (2)$$

where  $\Phi_i^q = -\sum_{j,i \neq j}^N T_{ij}^{q-q} q_j$  is the electrostatic potential on atom  $i$  due to the neighboring charges  $q_j$ ,  $\Phi_i^p = \sum_{j,i \neq j}^N \mathbf{T}_{ij}^{q-p} \mathbf{p}_j$  is the electrostatic potential on atom  $i$  due to the neighboring dipoles  $\mathbf{p}_j$ ,  $T_{ii}^{q-q}$  is the self-electrostatic potential for atom  $i$  to create a charge  $q_i$ , and  $\chi_i$  is the electron affinity of atom  $i$ . Equation (2) refers to the generation of electric charge  $q_i$  due to the various electrostatic potentials  $\Phi_i$  associated with atom  $i$ . From Eq. (2), we can calculate the electrostatic potential associated with each atom. By noting the

time-history of  $\Phi$  for every atom, we can estimate the voltage generated due to the crumpling deformation.

Figures 2(a)–2(c) show the atomic configuration colored using  $\Phi$  estimated from Eq. (2). In Fig. 2(a), initially, the inner atoms have  $\Phi = 1.258$  V and outer edge atoms have  $\Phi = 1.255$  V. The atoms near the boundary exhibit lower electrostatic fields than the central atoms. The structural changes due to indentation alter the local electric fields near the central portion of CGS, which results in highly localized changes in  $\Phi$  (about 4 mV reduction) from Figs. 2(a) to 2(b) due to the flexoelectric effect. Specifically, the initiation of the d-cone formation and increased bending in Fig. 2(b) leads to a change of hybridization (pyramidalization) from  $sp^2$  to  $sp^3$  for the atoms near the center, leading to a change in the bond angle from  $120^\circ$  to  $117^\circ$  with a 3% stretch in the bond lengths. These changes in the bond length and bond angles induce the observed inhomogeneity in  $\Phi$  that extends across the d-cone.

In Fig. 2(c), the core portion of the d-cone (labeled as O) shows a decrease of  $\Phi$  from 1.258 to 1.249 V of about 9 mV when compared to Fig. 2(a), where label A indicates the bin sector with maximal outward deflection, where  $\Phi$  rises 2 mV from 1.257 to 1.259 V.  $\overline{OA}$  represents the connecting line between bins O and A, which is used to define  $\theta$  to identify the relative positions of the other neighboring bins, as  $\theta = 0$  corresponds to  $\overline{OA}$ . From this line, the atomic deformation as well as changes in  $\Phi$  extends to the bins labeled as B and C, where the region between lines  $\overline{OB}$  and  $\overline{OC}$  covers the d-cone involved crumpled area. Near line  $\overline{OA}$ , the strain gradient-induced changes in the potential are clearly visible with respect to the d-cone folding [in Figs. 2(b) and 2(c)]. However, outside of this region, there are only small changes in potential due to the relatively small deformations of the graphene atoms in response to the indentation.

This is further verified by plotting the local curvature  $\kappa$  and  $\Phi$  across the different bin sectors defined from line  $\overline{OA}$ . The resulting

CGS curvature  $\kappa$  with  $\theta$  is shown in Fig. 3(a).  $\kappa$  is nearly constant for bins with small out-of-plane displacements, which occur for bins away from the d-cone. However,  $\kappa$  changes rapidly near the region where the d-cone forms. For  $r_p=8$  nm,  $\kappa$  shows an increase from  $-63^\circ$  to  $-30^\circ$  [corresponding atom bins are marked as B and D in Fig. 2(c) and in the inset of Fig. 4(a)]. The positive rise of  $\kappa$  between B to D corresponds to the left portion of the d-cone, where the out-of-plane ( $z$ ) deflections increase rapidly. From there  $\kappa$  decreases with increasing out-of-plane deflection and reaches a negative maxima at  $0^\circ$ , labeled as A, which corresponds to the d-cone region with the largest out-of-plane displacements [the central line of the d-cone O-A in Fig. 2(c)]. As  $\theta$  increases, an effectively symmetric response of  $\kappa$  is observed, with similar responses seen for CGS with radius 7, 9, and 10 nm.

Note that the choice of the calculation region radius  $r$  is 4 nm, which keeps the distance of separation between the bins O and A the same across the different sized CGS, while all atomic configurations were analyzed at  $\alpha_1 = 0.545$  to enable a consistent comparison for different CGS sizes. Importantly, we find that  $\theta_1$  is about  $62^\circ$  for all CGS we considered, which matches earlier theoretical and experimental results where  $\theta_1$  ranged from about  $60^\circ$ <sup>49</sup> to  $70^\circ$ <sup>50</sup>.

To further validate our simulations, we explore the response to indentation as a function of the dimensionless tip deflection  $\alpha_1$ . The core radius  $R_c$  is estimated from the locations of the bin sectors corresponding to the d-cone. The inset of Fig. 3(b) illustrates selected bins as red color dots. Note that we consider only the  $x$  and  $y$  coordinates for these bins. We then established a hyperbolic fitting<sup>51</sup> across the coordinate set [shown as a blue line in the inset of Fig. 3(b)], where  $R_c$  is the inverse curvature at the vertex of the fitted hyperbola. This process is repeated for the entire time-history of atomic configurations and all CGS systems. The variation of  $\alpha_2$  is nearly constant for  $\alpha_1$  less than 0.243 [Fig. 4(a)], which means that the indentation does not yield a

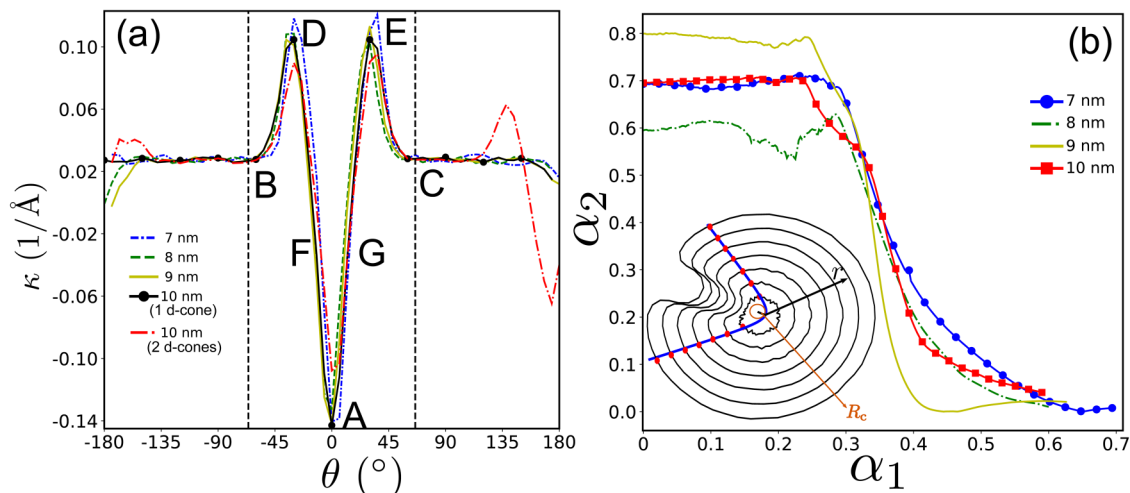


FIG. 3. (a) The variation of curvature  $\kappa$  with bin angle  $\theta$  for different  $r_p$  when  $\alpha_1 = 0.545$ , where the calculation region radius is 4 nm from O. (b) The variation of (a)  $\alpha_2$  or  $R_c$  with  $\alpha_1$  when  $r_p$  varies from 7 to 10 nm. The inset in (b) indicates the scheme for calculating core radius  $R_c$ . The blue line represents the fitting hyperbola.

significant deflection near the outer edges of the CGS. The initiation of out-of-plane  $z$  deflection leads to a decrease in the distance of separation between hyperbolic asymptotes, which leads to a decrease in the core radius. When  $\alpha_1$  is above 0.25,  $\alpha_2$  or  $R_c$  shows a decreasing trend in Fig. 3(b), which matches observed trends previously obtained for thin films.<sup>36</sup> These observations (Fig. 3) suggest that our MD simulation results for monolayer graphene match previous studies on d-cone formation in crumpled thin sheets.

## B. Flexoelectric voltage generation

Figure 4(a) shows the bin averaged potential difference  $\Phi - \Phi_O$  with respect to  $\theta$  when  $\alpha_1 = 0.545$  and where the calculation region radius is 4 nm from O. For the 8 and 9 nm CGS, the potential difference is constant for regions outside of the d-cone due to the small deformations there. From bins represented by labels B to D, there is a decrease in  $\Phi - \Phi_O$  of about 1 mV. In this region, the bond angle decreases by 0.110%, while the bond length increases by 0.363%. This increase in bond separation decreases the local electric fields, thus reducing the generated potential.

From region D to F,  $\Phi - \Phi_O$  reaches 12.336 mV, despite the average change in the bond length being only 0.033% and the average change in angle being only 0.115%. Thus, the large potential difference is driven by pyramidalization,<sup>52–54</sup> in which increased interactions between  $\pi$  and  $\sigma$  electrons take place due to increased curvature. Specifically, the changes in curvature tilt the  $\sigma$  bonds and break the symmetry in the  $\pi$  orbitals, which induces an electron transfer and creates local electric fields. The bond tilt changes the pyramidalization angle between the  $\sigma$  bonds to the  $\pi$  orbital axis vector, which is a function of bond angles between  $\sigma$  bonds.<sup>55</sup> The large in-plane electrical conductivity screens most of the generated in-plane electric fields, whereas there exist the out-of-plane electric fields that involve the generation of voltage

difference. For example, consider the CGS with  $r_p = 9$  nm at  $\alpha_1 = 0.462$ , where the total in-plane electric fields ( $E_x$  and  $E_y$ ) are about 30 times smaller than the out-of-plane electric field ( $E_z$ ). In total, the developed  $\pi - \sigma$  interactions increase the local electric fields and thus the potential  $\Phi$  for the associated atoms.

Between regions F and A, a 1.7 mV drop in the potential difference is observed. In this region, the large deformations increased the bond length by 0.614% and decreased the bond angle by 0.488%. The increase in the bond length again reduces the local electric fields and decreases the voltage in this region as shown in Fig. 4(a). Because the deformation of the d-cone is symmetric about  $\overline{OA}$ , the changes in potential going from A to G and G to E are similar to those previously discussed in going from D to F and F to A.

For the 7 nm CGS, in addition to the above observations, the atoms in the calculation region are impacted by edge atom effects, which cause an increase and then a decay in the developed potential difference from the d-cone edges to the other portion of the CGS. Overall, the variation of  $\Phi - \Phi_O$  is significant within  $\theta \leq |\theta_1|$ , which again indicates that the largest potential differences are confined to regions near the d-cone in Fig. 2(c). A zoom over one side of the d-cone [the inset of Fig. 4(a)] visualizes the voltage for bins A, B, D, and F more clearly.

For the 10 nm CGS, we found that the number of d-cones that a form exhibits some sensitivity to the initial conditions. For the 10 nm CGS with a single d-cone (marked as 1 d-cone), Fig. 4(a) shows that it exhibits similar behavior to the smaller CGS considered. However, the 10 nm CGS with multiple d-cones exhibits different behavior, which we now discuss. Specifically, for the 10 nm CGS with two d-cones, Fig. 4(a) (labeled as 2 d-cones) shows a 2 mV reduction in  $\Phi - \Phi_O$  between bins B to C, which is smaller than for the smaller radii CGS. In addition, we note there is a second rise in the potential difference starting from  $\theta > 113^\circ$ ,

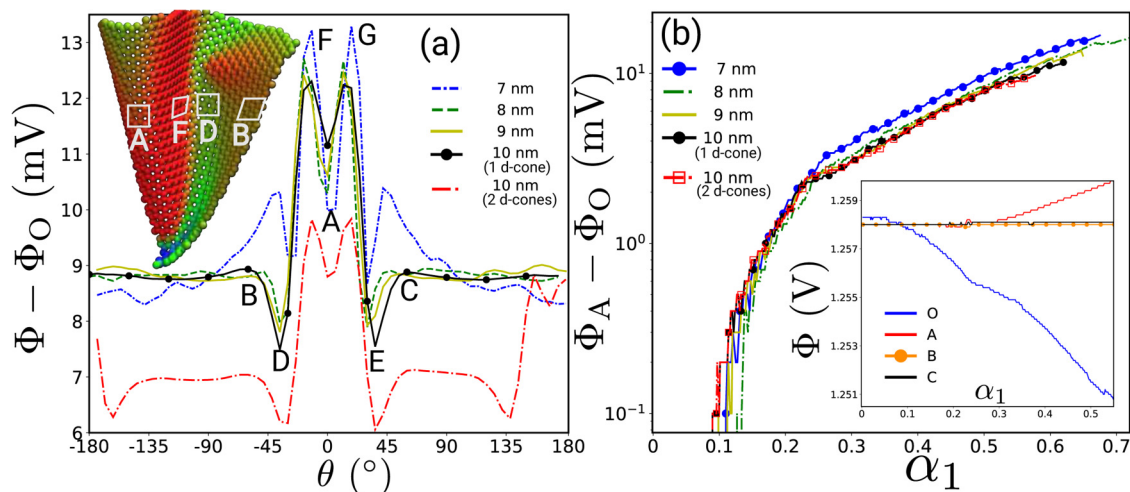


**FIG. 4.** (a) The variation of voltage  $\Phi - \Phi_O$  with bin angle  $\theta$  for different  $r_p$  when  $\alpha_1 = 0.545$ , where the calculation region radius is 4 nm from O. The inset in (a) indicates one side of the d-cone. Atomic coloring follows the color scale bar in Fig. 2. (b) The variation of  $\Phi_A - \Phi_O$  with  $\alpha_1$  when  $r_p$  varies from 7 to 10 nm. The inset in (b) represents the variation of  $\Phi$  with  $\alpha_1$  for 9 nm CGS.

which represents the generation of a secondary d-cone for the 10 nm CGS. The associated curvature changes in Fig. 3(a) (labeled as 2 d-cones) further supports this observation. The rise of the second d-cone further reduces the deformation near the central portion of the CGS, which makes the average potential for O for the 10 nm CGS to be 1.251 V whereas it is 1.248 V for the other CGS at the same  $\alpha_1$ . As a result, the total  $\Phi - \Phi_O$  is smaller for the 10 nm CGS with two d-cones as compared to the other CGS we considered. Figures 5(a) and 5(b) visualizes the atomic configurations for 10 nm CGS with the development of one and two d-cones. For the 10 nm CGS with two d-cones, the atoms associated with the secondary d-cone experienced enhanced charges, dipoles, and electrostatic fields, which can be viewed as enhanced  $\Phi$  for the atoms in the two d-cones in Fig. 5(b) when compared to Fig. 5(a). This is quantified using the comparison of energy densities between 9 and 10 nm CGS. For the 10 nm CGS with two d-cones at  $\alpha_1 = 0.545$ , the strain energy density is  $1.341 \times 10^{-6} \text{ J/m}^2$  and the electrical energy density is  $9.927 \times 10^{-6} \text{ J/m}^2$ . At nearly the same strain energy density, the 9 nm CGS yields  $4.871 \times 10^{-6} \text{ J/m}^2$  as the electrical energy density, which is 32% smaller than that in 10 nm case, which indicates the importance of the secondary d-cone. Although the average potential for the 10 nm CGS is lower compared to the 9 nm CGS, the increase of contribution from the secondary d-cone atoms increase the total electrical energy density.

To understand why the voltage  $\Phi - \Phi_O$  from the 10 nm CGS is smaller than the 9 nm CGS despite the generation of more electrical energy density due to the two d-cones, we consider atomic insights from bond stretching and changes in the bond angle. The average change in the bond length and bond angle for atoms between bins O and A for atomic configuration with  $\alpha_1 = 0.545$  is 0.074 Å and 0.438°, respectively, for the 10 nm CGS with two d-cones. For the 10 nm CGS with one d-cone, we find the average change in the bond length as 0.113 Å and the bond angle as 0.673°. For the 9 nm CGS at the same  $\alpha_1$ , these changes are 0.113 Å and 0.718°. The smaller changes in the atomic configuration for 10 nm CGS with two d-cones results in smaller strain gradients, and thus the resulting potential difference is lower as compared to the 10 nm CGS with one d-cone and the 9 nm CGS.

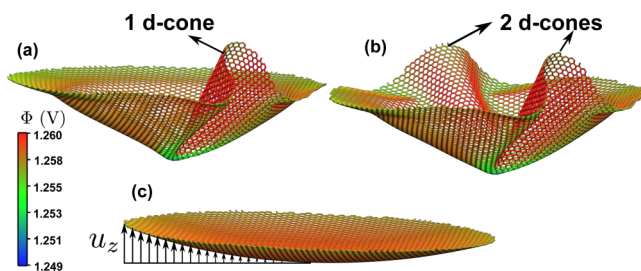


**FIG. 5.** Atomic snapshots of the indented CGS of radius 10 nm with (a) one d-cone (label 1 d-cone) and (b) two d-cones (label 2 d-cones). (c) Atomic view of 9 nm CGS under bending deformation. The radial increment of displacement field  $u_z$  represent the applied bending deformation. The visualized atomic configurations collected at the same strain energy density of  $1.341 \times 10^{-6} \text{ J/m}^2$ .

Figure 4(b) shows the variation of potential difference  $\Phi_A - \Phi_O$  with respect to  $\alpha_1$ . Here, we considered only the response of bin A, which contains the maximum deflections due to the d-cone, for studying the response with  $\alpha_1$ . For  $\alpha_1$  less than 0.1, there is no difference in the electrostatic potential between bins A and O. For  $\alpha_1$  between 0.1 and 0.3, as shown in the inset of Fig. 4(b), there is no observable change in potential for bin A. However, because the indenter deforms and stretches the atoms near the CGS center, this results in a decrease of  $\Phi_O$ , leading to an increase in potential difference  $\Phi_A - \Phi_O$ . Starting at  $\alpha_1 = 0.3$ ,  $\Phi_A$  begins increasing due to the formation of the d-cone. While the edges of the d-cone (bins B and C) show no changes in potential, this indicates the localization of deformation near the d-cone seen in Fig. 2(c). Further indentation leads to larger potential differences  $\Phi_A - \Phi_O$ , though the rate of potential increase decreases. These trends are observed for all CGS we simulated.

The observed voltage variation shows a similar trend with earlier theoretical predictions.<sup>36</sup> We note that the potential difference from our simulations on monolayer graphene is about 100 times smaller than the generated flexoelectric part of voltage from a poly vinylidene fluoride (PVDF) thin film. Thus, even though the flexoelectric constant for graphene ( $0.003 \text{ nC/m}^{12}$ ) is about 1000 times smaller than PVDF ( $13 \text{ nC/m}^{20}$ ), there is a 10 fold increase in the generation of voltage for crumpled graphene as compared to the scaled analytic theory. There are at least two important implications of this. First, this is likely due to the larger strain gradients that are possible at the nanoscale for a comparable deformation mode (d-cone based crumpling), which implies benefits of crumpling-based electromechanical energy conversion at the nanoscale. Furthermore, nanoscale systems can sustain such large strain gradients without creating atomic defects or cracks, which is beneficial for longer duration stability and durability. Finally, because other 2D materials such as the TMDCs have both a significantly larger flexoelectric constants and non-zero piezoelectric response as compared to graphene,<sup>12,13</sup> there may be additional enhancements in nanoscale flexoelectric energy generation through optimal material choices. Introducing the dopant mediated asymmetry in a composite material<sup>56,57</sup> may further help one to improve the flexoelectric effect under crumpling deformation.

### C. Benefits of crumpling for nanoscale flexoelectric energy generation

Finally, we discuss the potential benefits of crumpling graphene for nanoscale flexoelectric energy generation by comparing the response to the standard mode of flexoelectric energy generation, that of pure bending. To do so, we impose a displacement field  $u_z = \frac{1}{2}K(x^2 + y^2)$  to the atoms in the CGS, where  $K$  represents the strain gradient, and  $x$  and  $y$  represent the atom coordinates in the  $x$  and  $y$  directions. In these simulations, only the CGS is considered, i.e., there is no CNT indenter or hoop. A circular region of atoms with a radius greater than  $r_p - 0.5 \text{ nm}$  was selected as the boundary atoms for the given CGS with radius  $r_p$ ; these boundary atoms are fixed whereas all other atoms are allowed to relax due to the prescribed deformation for 1000 time steps under thermostat condition, the point charges and dipole moments are found for each atom using the charge-dipole model, after which

the local electric field and electrostatic potentials are also determined. Figure 5(c) shows the graphene atomic configuration under bending deformation.

Using this information, we compared the electrical energy density for atomic configurations at the same strain energy density for a 9 nm radius CGS deformed using crumpling and bending, following the bending methodology described in our previous works<sup>12,31</sup> as well as in recent experiments.<sup>25</sup> During the calculation of energy densities, we note that only the non-fixed interior atoms are used and the number of atoms is the same for both crumpling and bending simulations. The atomic configuration under crumpling deformation at  $\alpha_1 = 0.545$  gives an electrical energy density of  $4.871 \times 10^{-6} \text{ J/m}^2$  and a strain energy density of  $1.341 \times 10^{-6} \text{ J/m}^2$ . Selecting an atomic configuration for bending deformation of the 9 nm CGS with nearly the same strain energy density ( $1.381 \times 10^{-6} \text{ J/m}^2$ ) results in an electrical energy density  $1.5 \times 10^{-6} \text{ J/m}^2$ , which is about 70% lower than for crumpling.

The main difference between crumpling and bending is related to the strain gradients. For bending, the displacement field  $u_z$  is symmetric about the center of the CGS, which results in a uniform strain gradient, and thus lower electric fields, charges and dipole moments due to flexoelectricity. In crumpling, the out of plane deformation  $u_z$  is non-uniform about the CGS, and eventually results in the formation of a localized d-cone, which exhibits significant and non-uniform strain gradients, resulting in enhanced local electric fields and flexoelectric response yielding larger voltage generation. To quantify this, we first note that the voltage difference between bins A and O ( $\Phi_A - \Phi_O$ ) in the bending case is 0.566 mV, while it is 10.641 mV for crumpling. The average change in the bond length (0.009 Å) and the bond angle (0.336°) in bending are also lower compared to crumpling. We also calculated the potential difference  $\Phi_R - \Phi_O$ , where  $\Phi_R$  represents the average potential for all atoms besides the boundary atoms and those in bin O. This difference is 1.52 mV for bending and 8.41 mV for crumpling, again demonstrating the significant increase in flexoelectric energy generation for crumpling compared to bending. Overall, this shows that the uniform strain gradient from bending results in less localized deformation, strain gradients, and thus generated flexoelectric voltage than crumpling.

#### IV. CONCLUSION

We utilized classical molecular dynamics coupled with the charge-dipole model to investigate the potential of flexoelectric energy generation in graphene, the model 2D nanomaterial, due to crumpling deformations. After verifying that our simulations qualitatively reproduced previous predictions for d-cone characteristics, including core radius and non-dimensional indentation depth, we examined the mechanisms controlling the flexoelectric energy conversion. First, we found that the voltage generated by crumpling graphene is about an order of magnitude higher than is expected from scaling macroscale relationships down to the nanoscale, indicating the benefit of exploiting large strain gradients that are possible in nanomaterials. Second, we found that the electrical energy density and voltage generated in crumpling significant exceeds that observed in bending, which implies the benefits of crumpling rather than bending nanomaterials to maximize the flexoelectric

effect. Finally, we anticipate that other 2D materials, such as the TMDCs, will exhibit superior flexoelectric energy generation under crumpling as compared to graphene; we plan to present such comparisons in future work.

#### ACKNOWLEDGMENTS

X. Zhuang would like to acknowledge the ERC Starting Grant (No. 802205) and NSFC (No. 11772234).

#### DATA AVAILABILITY

The data that support the findings of this study are available from the corresponding authors upon reasonable request.

#### REFERENCES

- 1E. Pop, V. Varshney, and A. K. Roy, "Thermal properties of graphene: Fundamentals and applications," *MRS Bull.* **37**(12), 1273–1281 (2012).
- 2S. Ghosh, W. Bao, D. L. Nika, S. Subrina, E. P. Pokatilov, C. N. Lau, and A. A. Balandin, "Dimensional crossover of thermal transport in few-layer graphene," *Nat. Mater.* **9**(7), 555 (2010).
- 3R. Fei and L. Yang, "Strain-engineering the anisotropic electrical conductance of few-layer black phosphorus," *Nano Lett.* **14**(5), 2884–2889 (2014).
- 4S. Yu, X. Wu, Y. Wang, X. Guo, and L. Tong, "2D materials for optical modulation: Challenges and opportunities," *Adv. Mater.* **29**(14), 1606128 (2017).
- 5Q. H. Wang, K. Kalantar-Zadeh, A. Kis, J. N. Coleman, and M. S. Strano, "Electronics and optoelectronics of two-dimensional transition metal dichalcogenides," *Nat. Nanotechnol.* **7**(11), 699 (2012).
- 6P. Z. Hanakata, A. Carvalho, D. K. Campbell, and H. S. Park, "Polarization and valley switching in monolayer group-IV monochalcogenides," *Phys. Rev. B* **94**(3), 035304 (2016).
- 7R. C. Andrew, R. E. Mapasha, A. M. Ukpong, and N. Chetty, "Mechanical properties of graphene and boronitrene," *Phys. Rev. B* **85**(12), 125428 (2012).
- 8B. Javvaji, P. Budarapu, V. Sutrarakar, D. R. Mahapatra, M. Paggi, G. Zi, and T. Rabczuk, "Mechanical properties of graphene: Molecular dynamics simulations correlated to continuum based scaling laws," *Comput. Mater. Sci.* **125**, 319–327 (2016).
- 9S. J. Kim, K. Choi, B. Lee, Y. Kim, and B. H. Hong, "Materials for flexible, stretchable electronics: Graphene and 2D materials," *Annu. Rev. Mater. Res.* **45**, 63–84 (2015).
- 10Z. Sun, A. Martinez, and F. Wang, "Optical modulators with 2D layered materials," *Nat. Photonics* **10**(4), 227 (2016).
- 11R. Mas-Ballesté, C. Gómez-Navarro, J. Gómez-Herrero, and F. Zamora, "2D materials: To graphene and beyond," *Nanoscale* **3**(1), 20–30 (2011).
- 12X. Zhuang, B. He, B. Javvaji, and H. S. Park, "Intrinsic bending flexoelectric constants in two-dimensional materials," *Phys. Rev. B* **99**(5), 054105 (2019).
- 13B. Javvaji, B. He, X. Zhuang, and H. S. Park, "High flexoelectric constants in Janus transition-metal dichalcogenides," *Phys. Rev. Mater.* **3**(12), 125402 (2019).
- 14L. J. McGilly, A. Kerelsky, N. R. Finney, K. Shapovalov, E.-M. Shih, A. Ghiotto, Y. Zeng, S. L. Moore, W. Wu, Y. Bai, K. Watanabe, T. Taniguchi, M. Stengel, L. Zhou, J. Hone, X. Zhu, D. N. Basov, C. Dean, C. E. Dreyer, and A. N. Pasupathy, "Visualization of Moiré superlattices," *Nat. Nanotechnol.* **15**(7), 580–584 (2020).
- 15V. I. Artyukhov, S. Gupta, A. Kutana, and B. I. Yakobson, "Flexoelectricity and charge separation in carbon nanotubes," *Nano Lett.* **20**(5), 3240–3246 (2020).
- 16B. Mortazavi, B. Javvaji, F. Shojaei, T. Rabczuk, A. V. Shapeev, and X. Zhuang, "Exceptional piezoelectricity, high thermal conductivity and stiffness and promising photocatalysis in two-dimensional MoSi<sub>2</sub>N<sub>4</sub> family confirmed by first-principles," *Nano Energy* **82**, 105716 (2021).
- 17S. Kumar, D. Codony, I. Arias, and P. Suryanarayana, "Flexoelectricity in atomic monolayers from first principles," *Nanoscale* **13**(3), 1600–1607 (2021).

- <sup>18</sup>T. Pandey, L. Covaci, and F. Peeters, "Tuning flexoelectricity and electronic properties of zig-zag graphene nanoribbons by functionalization," *Carbon* **171**, 551–559 (2021).
- <sup>19</sup>J.-W. Jiang, Z. Qi, H. S. Park, and T. Rabczuk, "Elastic bending modulus of single-layer molybdenum disulfide (MoS<sub>2</sub>): Finite thickness effect," *Nanotechnology* **24**(43), 435705 (2013).
- <sup>20</sup>Q. Deng, M. Kammoun, A. Erturk, and P. Sharma, "Nanoscale flexoelectric energy harvesting," *Int. J. Solids Struct.* **51**(18), 3218–3225 (2014).
- <sup>21</sup>R. Hinchet, U. Khan, C. Falconi, and S.-W. Kim, "Piezoelectric properties in two-dimensional materials: Simulations and experiments," *Mater. Today* **21**(6), 611–630 (2018).
- <sup>22</sup>C. Cui, F. Xue, W. J. Hu, and L. J. Li, "Two-dimensional materials with piezoelectric and ferroelectric functionalities," *npj 2D Mater. Appl.* **2**(1), 18 (2018).
- <sup>23</sup>M. B. Ghasemian, T. Daeneke, Z. Shahrabaki, J. Yang, and K. Kalantar-Zadeh, "Peculiar piezoelectricity of atomically thin planar structures," *Nanoscale* **12**, 2875–2901 (2020).
- <sup>24</sup>B. Wang, Y. Gu, S. Zhang, and L.-Q. Chen, "Flexoelectricity in solids: Progress, challenges, and perspectives," *Prog. Mater. Sci.* **106**, 100570 (2019).
- <sup>25</sup>X. Wang, A. Cui, F. Chen, L. Xu, Z. Hu, K. Jiang, L. Shang, and J. Chu, "Probing effective out-of-plane piezoelectricity in van der Waals layered materials induced by flexoelectricity," *Small* **15**(46), 1903106 (2019).
- <sup>26</sup>D. Tan, M. Willatzen, and Z. L. Wang, "Out-of-plane polarization in bent graphene-like zinc oxide and nanogenerator applications," *Adv. Funct. Mater.* **30**(5), 1907885 (2020).
- <sup>27</sup>M. Willatzen, P. Gao, J. Christensen, and Z. L. Wang, "Acoustic gain in solids due to piezoelectricity, flexoelectricity, and electrostriction," *Adv. Funct. Mater.* **30**, 2003503 (2020).
- <sup>28</sup>K. P. Dou, H. H. Hu, X. Wang, X. Wang, H. Jin, G.-P. Zhang, X.-Q. Shi, and L. Kou, "Asymmetrically flexoelectric gating effect of Janus transition-metal dichalcogenides and their sensor applications," *J. Mater. Chem. C* **8**, 11457–11467 (2020).
- <sup>29</sup>D. Bennett, "Flexoelectric-like radial polarization of single-walled nanotubes from first-principles," *Electron. Struct.* **3**, 015001 (2021).
- <sup>30</sup>S. Chandratte and P. Sharma, "Coaxing graphene to be piezoelectric," *Appl. Phys. Lett.* **100**(2), 12–15 (2012).
- <sup>31</sup>B. Javvaji, B. He, and X. Zhuang, "The generation of piezoelectricity and flexoelectricity in graphene by breaking the materials symmetries," *Nanotechnology* **29**(22), 225702 (2018).
- <sup>32</sup>R. Gleiter, "Pi-sigma interactions: Experimental evidence and its consequences for the chemical reactivity of organic compounds," *Pure Appl. Chem.* **59**(12), 1585–1594 (1987).
- <sup>33</sup>S. Park, J. Park, Y.-G. Kim, S. Bae, T.-W. Kim, K.-I. Park, B. H. Hong, C. K. Jeong, and S.-K. Lee, "Laser-directed synthesis of strain-induced crumpled MoS<sub>2</sub> structure for enhanced triboelectrification toward haptic sensors," *Nano Energy* **78**, 105266 (2020).
- <sup>34</sup>F. J. Maier, M. Schneider, J. Schratzenholzer, W. Artner, K. Hradil, A. Artemenko, A. Kromka, and U. Schmid, "Flexoelectricity in polycrystalline TiO<sub>2</sub> thin films," *Acta Mater.* **190**, 124–129 (2020).
- <sup>35</sup>P. Kodali, G. Saravanel, and S. Sambandan, "Crumpling for energy: Modeling generated power from the crumpling of polymer piezoelectric foils for wearable electronics," *Flexible Printed Electron.* **2**, 035005 (2017).
- <sup>36</sup>B. Wang, S. Yang, and P. Sharma, "Flexoelectricity as a universal mechanism for energy harvesting from crumpling of thin sheets," *Phys. Rev. B* **100**, 035438 (2019).
- <sup>37</sup>S. J. Stuart, A. B. Tutein, and J. A. Harrison, "A reactive potential for hydrocarbons with intermolecular interactions," *J. Chem. Phys.* **112**(14), 6472–6486 (2000).
- <sup>38</sup>A. Mayer, "Polarization of metallic carbon nanotubes from a model that includes both net charges and dipoles," *Phys. Rev. B* **71**(23), 235333 (2005).
- <sup>39</sup>A. Mayer, "Formulation in terms of normalized propagators of a charge-dipole model enabling the calculation of the polarization properties of fullerenes and carbon nanotubes," *Phys. Rev. B* **75**(4), 045407 (2007).
- <sup>40</sup>S. Plimpton, "Fast parallel algorithms for short-range molecular dynamics," *J. Comput. Phys.* **117**(1), 1–19 (1995).
- <sup>41</sup>W. Humphrey, A. Dalke, and K. Schulten, "VMD: Visual molecular dynamics," *J. Mol. Graph.* **14**(1), 33–38 (1996).
- <sup>42</sup>W. Jiang, Y. Zeng, Q. Qin, and Q. Luo, "A novel oscillator based on heterogeneous carbon@MoS<sub>2</sub> nanotubes," *Nano Res.* **9**(6), 1775–1784 (2016).
- <sup>43</sup>S. Nosé, "A unified formulation of the constant temperature molecular dynamics methods," *J. Chem. Phys.* **81**(1), 511–519 (1984).
- <sup>44</sup>W. G. Hoover, "Canonical dynamics: Equilibrium phase-space distributions," *Phys. Rev. A* **31**(3), 1695–1697 (1985).
- <sup>45</sup>W. C. Swope, H. C. Andersen, P. H. Berens, K. R. Wilson, W. C. Swope, H. C. Andersen, P. H. Berens, and K. R. Wilson, "A computer simulation method for the calculation of equilibrium constants for the formation of physical clusters of molecules: Application to small water clusters," *J. Chem. Phys.* **76**, 637–649 (1982).
- <sup>46</sup>S. Chen, S. Gonella, W. Chen, and W. K. Liu, "A level set approach for optimal design of smart energy harvesters," *Comput. Methods Appl. Mech. Eng.* **199**(37–40), 2532–2543 (2010).
- <sup>47</sup>S. S. Nanthakumar, T. Lahmer, X. Zhuang, H. S. Park, and T. Rabczuk, "Topology optimization of piezoelectric nanostructures," *J. Mech. Phys. Solids* **94**, 316–335 (2016).
- <sup>48</sup>A. Homayouni-Amlashi, T. Schlinquer, A. Mohand-Ousaid, and M. Rakotondrabe, "2D topology optimization MATLAB codes for piezoelectric actuators and energy harvesters," *Struct. Multidiscipl. Optim.* **63**(2), 983–1014 (2021).
- <sup>49</sup>S. Chaïeb, F. Melo, and J.-C. Géninard, "Experimental study of developable cones," *Phys. Rev. Lett.* **80**(11), 2354–2357 (1998).
- <sup>50</sup>E. Cerda and L. Mahadevan, "Conical surfaces and crescent singularities in crumpled sheets," *Phys. Rev. Lett.* **80**(11), 2358–2361 (1998).
- <sup>51</sup>T. Liang and T. A. Witten, "Crescent singularities in crumpled sheets," *Phys. Rev. E* **71**(1), 016612 (2005).
- <sup>52</sup>T. Dumitrică, C. M. Landis, and B. I. Yakobson, "Curvature-induced polarization in carbon nanoshells," *Chem. Phys. Lett.* **360**(1–2), 182–188 (2002).
- <sup>53</sup>V. J. Surya, K. Yakutti, H. Mizuseki, and Y. Kawazoe, "Modification of graphene as active hydrogen storage medium by strain engineering," *Comput. Mater. Sci.* **65**, 144–148 (2012).
- <sup>54</sup>I. Nikiforov, E. Dontsova, R. D. James, and T. Dumitrică, "Tight-binding theory of graphene bending," *Phys. Rev. B* **89**(15), 1–13 (2014).
- <sup>55</sup>R. C. Haddon, "Comment on the relationship of the pyramidalization angle at a conjugated carbon atom to the  $\sigma$  bond angles," *J. Phys. Chem. A* **105**(16), 4164–4165 (2001).
- <sup>56</sup>H. Ghasemi, H. S. Park, and T. Rabczuk, "A multi-material level set-based topology optimization of flexoelectric composites," *Comput. Methods Appl. Mech. Eng.* **332**, 47–62 (2018).
- <sup>57</sup>S. I. Kundalwal, V. K. Choyal, N. Luhadiya, and V. Choyal, "Effect of carbon doping on electromechanical response of boron nitride nanosheets," *Nanotechnology* **31**(40), 405710 (2020).